Yamaya *et al. Earth, Planets and Space (2022) 74:164*
https://doi.org/10.1186/s40623-022-01721-3

Earth, Planets and Space

FULL PAPER

Open Access

CMT inversion for small-to-moderate earthquakes applying to dense short-period OBS array at off Ibaraki region

Lina Yamaya[1,2*], Kimihiro Mochizuki[1], Takeshi Akuhara[1], Shunsuke Takemura[1], Masanao Shinohara[1] and Tomoaki Yamada[1]

Abstract

We conducted centroid moment tensor (CMT) inversion for small-to-moderate aftershocks in the off Ibaraki region of the 2011 off the Pacific coast of Tohoku earthquake. In this study, we used high-frequency (0.4–1.0 Hz) seismograms from a dense array of short-period ocean bottom seismometers (OBSs) and a reliable three-dimensional (3-D) seismic velocity model. Higher frequency analysis and dense OBS arrays offer CMT solutions with high spatial resolutions. Since our OBS array observed aftershocks occurring immediately following the 2011 off the Pacific coast of Tohoku earthquake, we determined 536 CMT solutions for small-to-moderate aftershocks in the off Ibaraki region (JMA-scale magnitudes of 2.5–4.0). According to our CMT solutions, characteristics of the aftershock activities in the off Ibaraki region are classified into 5 groups: (1) thrust earthquakes, which are considered as interplate earthquakes, separated by the large slip area of the 2011 Ibaraki-oki earthquake (the largest M_W 7.6 aftershock of the 2011 off the Pacific coast of Tohoku earthquake) and the tectonic tremors; (2) intraslab strike-slip earthquakes located at the north of the fault area of the 2011 Ibaraki-oki earthquake; (3) intraslab normal-fault earthquakes, which suggest a tensional stress field within the subducting Pacific Plate due to the plate bending by the overriding Philippine Sea Plate; (4) various earthquake focal mechanisms above a subducting seamount, which suggest the 3-D complex fractures; and (5) normal-fault earthquakes shallower than the interplate earthquakes, which were possibly caused by the heterogeneity of the subducting seamount.

Keywords: CMT inversion, Ocean bottom seismometer, Focal mechanism, Off Ibaraki, The 2011 off the Pacific coast of Tohoku earthquake

*Correspondence: lina@bosai.go.jp

[1] Earthquake Research Institute, The University of Tokyo, 1-1-1, Yayoi, Tokyo, Bunkyo-Ku, Japan
Full list of author information is available at the end of the article

Graphical Abstract

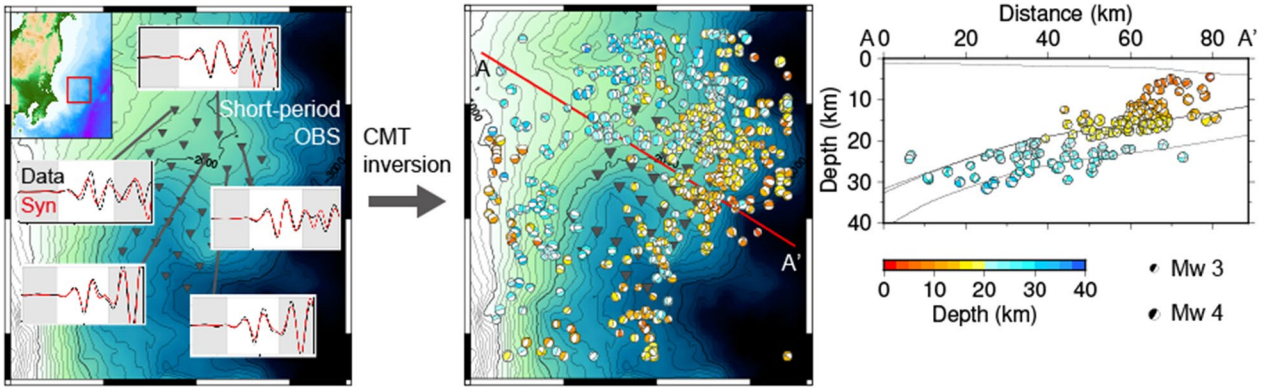

Introduction

Determining earthquake focal mechanisms is important for understanding the earthquake source mechanisms and tectonic stress fields. The off Ibaraki region (Fig. 1a), northeastern Japan, in the Japan Trench subduction zone, is expected to be characterized by a heterogeneous stress field. In addition to the Pacific Plate subducting beneath the northeastern Japan from the east, the Philippine Sea Plate is subducting on the Pacific Plate. The northeastern edge of the Philippine Sea plate has been estimated in this region (green line in Fig. 1a, e.g., Uchida et al. 2010; Nakahigashi et al. 2012). Tectonic loading from the 2 subducting plates complicates the stress field. On the incoming Pacific Plate seaward of the trench, a chain of seamounts exists. Mochizuki et al. (2008) has identified a subducting seamount with a width of ~ 50 km and a height of ~ 3 km in this region. The influence of subducting seamounts on the stress field and seismicity is not yet clear, although it has long been discussed through geological or numerical experiments (e.g., Wang and Bilek 2011, 2014; Sun et al. 2020). Moreover, this region lies around the southern limit of the 2011 off the Pacific coast of Tohoku earthquake (hereafter, we referred to as "the 2011 Tohoku-oki earthquake") with M_w 9.0. The largest M_w 7.6 aftershock (the 2011 Ibaraki-oki earthquake) occurred approximately 30 min after the 2011 Tohoku-oki earthquake. Static stress changes caused by large earthquakes also affect the stress field and seismicity around the fault area (e.g., Hasegawa et al. 2012; Yoshida et al. 2014). Thus, the off Ibaraki region is an important study area for the seismicity and the stress field related to plate subduction, seamounts, and large earthquakes.

Despite these situations, focal mechanism catalogs were not sufficient with respect to their spatio-temporal densities and resolutions in the off Ibaraki region, which decreases the statistical stability and the resolution in the analysis of the stress field. In Japan, focal mechanism catalogs of regional centroid moment tensor (CMT) solutions (e.g., F-net moment tensor (MT): Fukuyama et al. 1998; Kubo et al. 2002; Accurate and QUick Analysis system for source parameters (AQUA) CMT: Matsumura et al. 2006) and first-motion solutions compiled by the Japan Meteorological Agency (JMA) have been routinely determined and contributing to studying the stress field. Some studies redetermined CMT solutions in the Tohoku region to discuss the stress field before and after the Tohoku-oki earthquake (e.g., Asano et al. 2011; Lister et al. 2018). However, any of the systems cannot determine focal mechanisms for $M_w \leq 3.5$ offshore earthquakes. In addition, even for earthquakes with M_w of 3.5–4.0, it is difficult to determine the focal mechanisms of all detected offshore earthquakes. This is because of the low signal-to-noise ratio for low-frequency (e.g., 0.02–0.05 Hz) surface waves and high-frequency first-arrivals at onshore stations. This limited capability of analyzing small earthquakes reduces the number of obtained focal mechanisms, which decreases their spatio-temporal densities. The only use of onshore network data also reduces the spatial resolution of hypocenter determination in offshore regions owing to their far epicentral distances and insufficient azimuthal coverage. In addition, the spatial resolutions of those MT/CMT solutions based on low-frequency surface waves are not sufficient owing to their wavelengths.

Other than the established focal mechanism catalogs, studies using temporally deployed short-period ocean bottom seismometers (OBSs) generally determined first-motion focal mechanisms (e.g., Shinohara et al., 2012; Obana et al. 2021). However, only a few first-motion focal mechanisms were determined in the off Ibaraki region by a series of OBS observations, including the OBS array used in the present study (Shinohara et al. 2012). This

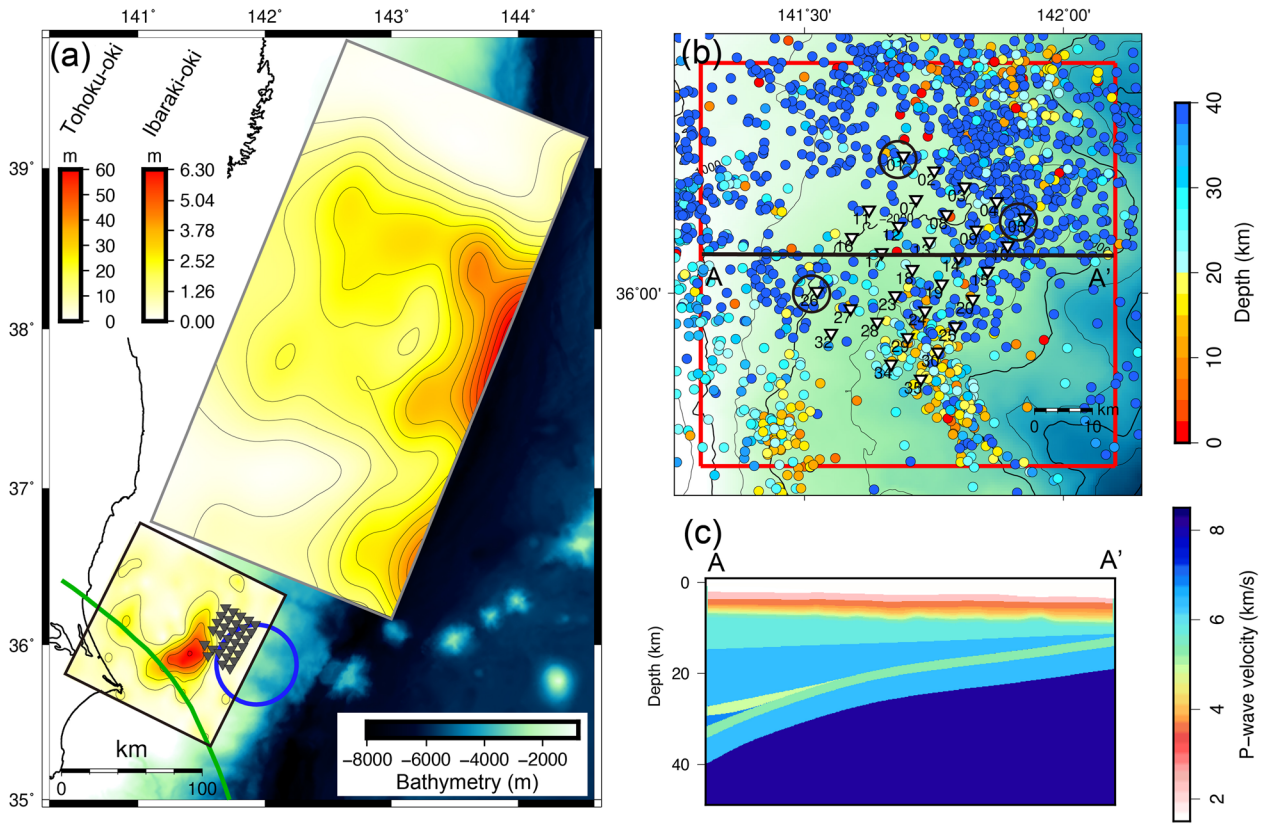

Fig. 1 **a** Study area with the slip distribution of the 2011 Tohoku-oki earthquake within a grey square (Lay et al. 2011), as well as the 2011 Ibaraki-oki earthquake within a black square (Kubo et al. 2013). The grey triangles show the stations of the OBS array in the off Ibaraki region. The blue circle shows the subducting seamount (Mochizuki et al. 2008). The green line shows the northeastern limit of the Philippine Sea Plate (Uchida et al. 2010). **b** Distribution of seismicity and OBS stations. The white triangles show OBS stations. The circled white triangles show the stations which were recovered approximately 2 weeks after the 2011 Tohoku-oki earthquake occurred. The colored circles show the earthquake hypocenters determined by JMA with their color indicating their depth. The red rectangle represents the region, where the Green's functions were calculated. **c** Seismic velocity structure model along profile A–A' in (**b**). The region shallower than ~ 10 km was constructed by Yamaya et al. (2021), and deeper by Koketsu et al. (2012)

limitation is possibly because of a low signal-to-noise ratio due to S and coda waves of the intense aftershock activity, which obstructs manual phase identifications for reading the first-motion polarities. These technical difficulties in estimating the focal mechanisms for offshore small-to-moderate earthquakes must be overcome to elucidate the detailed aftershock activity and stress field in the off Ibaraki region.

Therefore, we apply CMT inversions to high-frequency (0.4–1.0 Hz) body-wave data obtained from a dense array of short-period OBSs. CMT inversion can include information on the amplitudes and phases, in addition to the first-motion polarities. Moreover, manual phase identification is not required in typical grid-search CMT methods. Despite the advantages of CMT inversion, analysis of waveform data from OBS networks, such as CMT inversion, has still been limited in offshore region. Oceanic sediments and seawater layers strongly affect seismic wave propagation (e.g., Shapiro et al. 1998; Nakamura et al. 2015; Noguchi et al. 2016; Volk et al. 2017). Especially in subduction zones or large sedimentary basins with heterogeneous bedrock topography, 3-D seismic velocity structure models are needed to obtain accurate CMT solutions (e.g., Hejrani et al. 2017, 2019, 2020; Takemura et al. 2020; Wang and Zhan 2020; White et al. 2019). To accurately obtain CMT solutions of offshore earthquakes with smaller magnitudes, the use of an appropriate seismic velocity structure model and analysis of higher frequency seismograms should be incorporated. Such CMT analysis has become possible through recent developments in detailed seismic velocity models, numerical simulation codes of seismic wave propagation, and computational resources.

In this study, we conduct CMT inversions of M_W2.5–4.5 aftershocks of the 2011 Tohoku-oki earthquake in the off Ibaraki region. To achieve higher spatial resolutions of CMT solutions, we use P-wave data filtered with 0.4–1.0 Hz from the dense OBS array and Green's functions with a 3-D seismic velocity structure model. The dense array and higher frequency analysis significantly increase the spatial resolution of the CMT solutions. The obtained CMT solutions reflect heterogeneous stress field in the off Ibaraki region related to tectonic loading from the Pacific Plate and the Philippine Sea Plate, the subducting seamount, and the 2011 Ibaraki-oki earthquake.

Data

This study used velocity seismograms from a dense array with 30 OBSs deployed in the off Ibaraki region, in northeastern Japan along the Japan Trench subduction zone (Fig. 1a). The OBS array is composed of three-component short-period (1 Hz) seismometers (LE-3Dlite, Lennartz) with station intervals of approximately 6 km (Fig. 1b). First, 24 OBSs near the array center were deployed on October 17, 2010, and the surrounding 11 OBSs were added on February 14, 2011. After the observation started, on March 11, the 2011 Tohoku-oki earthquake occurred. Three of the OBSs were recovered about 2 weeks after the 2011 Tohoku-oki earthquake to investigate the aftershock activity. Of the OBSs, 28 were recovered in September 2011, but one of the recovered OBSs had an erroneously low amplitude level, likely due to a malfunction of its recorder.

To conduct CMT inversions of small-to-moderate earthquakes in the off Ibaraki region, we selected earthquakes with JMA-scale magnitudes (M_{JMA}) of 2.5–4.0 that occurred within the region covering from 141.3°E to 142.1°E and from 35.7°N to 36.4°N. We used the earthquakes that occurred following the 2011 Tohoku-oki earthquake and before September 17, 2011.We note that the seismicity was low in this region before the 2011 Tohoku-oki earthquake, according to the JMA and F-net MT catalogs.

Methods

For CMT inversion in this study, we used the seismic records of P-waves on the vertical component. The signal-to-noise ratios on the horizontal components were insufficient for the P-waves. We adopted a frequency range of 0.4–1.0 Hz (i.e., P-wave wavelengths of 2–5 km assuming P-wave velocity of 5 km/s). This is because observed seismograms from our short-period OBSs have little sensitivity at a frequency lower than 0.4 Hz, and the determined CMTs from higher frequency seismograms can be expected to have higher spatio-temporal resolutions (e.g., Hejrani & Tkalčić, 2020; Wang & Zhan 2020). At a frequency higher than approximately 1.0 Hz, the incoherently scattered wavefield becomes dominant (e.g., Takemura et al. 2016; Sato et al. 2012). We did not use S-waves, because most seismograms were saturated for earthquakes with $M_w > 3.5$.

Green's functions were calculated using the Open-source Seismic Wave Propagation Code (OpenSWPC; Maeda et al. 2017) based on the staggered-grid finite difference method (FDM). We used the reciprocal method to obtain Green's functions at 30 stations from 494710 assumed source grids efficiently. The reciprocal method has been used in previous CMT inversion studies, where the number of the source grid points was significantly larger than that of the stations (e.g., Hejrani et al. 2017; Okamoto et al. 2018; Wang and Zhang. 2020). The source grids were set at an interval of 0.01° (~0.6 km) within the regions from 141.3°E to 142.1°E and from 35.7°N to 36.4°N (Fig. 1b). Those along the depth were distributed from 0 to 45 km with an interval of 0.5 km. In the reciprocal calculations, a model volume of $90 \times 90 \times 50\text{km}^3$ was discretized with a uniform grid interval of 0.025 km. We calculated 40 s of Green's functions using 32,000 time-steps. We assumed the source time function as a Küpper wavelet with a duration of 0.1 s, which exhibits a flat response in our frequency range (see Fig. 4 of Maeda et al. 2017). Some of the target earthquakes with $\geq M_W4.0$ may have source time functions with durations of about 1.0 s, which may affect seismogram durations in our target frequencies. Using our synthetic waveforms and a moment–duration relationship (Eq. (1) of Ekström et al. 2012), we confirmed that the effects of finite-duration source time functions are expected to be negligible for earthquakes with $M_w < 4.5$ (Additional file 1: Fig. S1). The reciprocal calculations of Green's functions were conducted using the Oakforest-PACS system at the Information Technology Center, The University of Tokyo. Each calculation needs 5.1 Tbyte memory and a wall-clock time of 2.5 h with 512-node (33792 cores) parallel computing.

Beneath this region, the Pacific Plate is subducting from the east. Offshore seismic surveys (e.g., Tsuru et al. 2002; Mochizuki et al. 2008) and ambient noise studies (e.g., Yamaya et al. 2021) suggest the existence of ~2 km oceanic sediments at shallower depths. To accurately model seismic wave propagation at the off Ibaraki region, we used a 3-D seismic velocity structure model. We constructed the 3-D model (Fig. 1c) by combining structures beneath the lower crust from the Japan Integrated Velocity Structure Model (JIVSM; Koketsu et al. 2012) and above the lower crust from a detailed local structure (Yamaya et al. 2021). The JIVSM is widely used for CMT inversions

from low-frequency (<∼ 0.25 Hz) seismograms (e.g., Okamoto et al. 2018; Takemura et al. 2020, 2021) for evaluating long-period hazard maps for Japan (https://www.jishin.go.jp/evaluation/seismic_hazard_map/lpshm/12_choshuki/). Here, we note that the Pacific Plate of the JIVSM roughly agrees with other studies of active-source seismic surveys (e.g., Tsuru et al. 2002; Mochiuki et al. 2008; Nakahigashi et al. 2012). Yamaya et al. (2021) resolved the fine-scale S-wave velocity structure of the sediments and the upper crust of the off Ibaraki region with resolutions of ∼ 0.1–1.0 km vertically and ∼ 10 km horizontally. Our sedimentary structure model can be downloaded from https://doi.org/10.5281/zenodo.6999136. The lowest S-wave velocity in our calculations is 0.34 km/s, and consequently, our FDM calculations can precisely simulate seismic wave propagation for our CMT inversion. Such high-resolution 3-D structures possibly increase CMT resolutions (e.g., Hejrani & Tkalčić, 2020; Wang & Zhan 2020). We assumed P-wave velocity and density structures through the empirical scaling law using Eqs. (1) and (9) in Brocher (2005). Although this scaling law does not consider unconsolidated sediments, the predicted P-wave velocity from the very low S-wave velocity (0.34 km/s) is 1.57 km/s. This obtained P-wave velocity is consistent with those obtained by active-source surveys at the off Ibaraki region (e.g., Mochizuki et al. 2008) and by the Ocean Drilling Program at Japan Trench off northeast Japan (Shipboard Scientific Party 2000). We also assumed the anelastic attenuation Q values using the empirical scaling law by Eqs. (5) and (7) in Brocher (2008). Other technical details (e.g., seawater, air layer, and boundary conditions) are the same as shown in Maeda et al. (2017).

We applied the P-wave time windows for the CMT inversions as follows: for each source grid, we selected the P-wave arrivals of the synthetic seismograms when these absolute amplitudes first exceeded 5% of the maximum absolute amplitude. Then, we determined a 3-s time window starting 1.5 s before the P-wave arrival. We applied the same time window to the observed seismograms. The data saturated within 5 s from the beginning of the time window were excluded from the analysis. Because the lower frequency data (< 0.4 Hz) are less sensitive to the earthquake signal than the instrumental noise at the short-period OBS, we convolved the synthetic seismograms with the instrumental response function. We note that we did not remove the instrumental response with deconvolution, because the increased instrumental noises for lower frequency components were significantly enhanced, and consequently, earthquake signals were contaminated by these noises.

To constrain the grid-search range of the centroid location for CMT inversion, we determined an initial centroid location. The initial centroid location and time were roughly determined from the P-wave arrival times by a grid search. For this purpose, we automatically detected the arrival times of observed seismograms using the kurtosis gradient functions (e.g., Langet et al. 2014) applied to the waveform data filtered between 4.0 and 10.0 Hz (Additional file 1: Fig. S2). The redetermined hypocenters and origin times were consistent with those of Shinohara et al. (2011, 2012), but differed from those routinely determined by JMA, which relied solely on onshore stations.

We selected Green's functions at the source grids located horizontally within a 0.24°× 0.24° rectangle centered on the initial hypocenter and vertically within depths of 1–45 km. The grid search for centroid time was conducted at every 0.1 s within -1 to 1 s from the initial centroid time, which is the redetermined origin time. Note that we did not apply any station corrections, such as shifting the time window differently for each station as used in the previous studies of hypocenter relocations with the OBSs (e.g., Shinohara et al. (2011, 2012).

A moment tensor inversion was conducted for each spatial and temporal grid. In this study, we fixed the isotropic component of the moment tensor to be zero. Following Sipkin (1982), the seismogram of the kth station is written as

$$u_k(t) = \sum_{n=1}^{5} m_n * G_{kn}(t), \tag{1}$$

where m_n is the nth component of the moment tensor, and $G_{kn}(t)$ is Green's functions. We solved this equation using the least-squares method and then calculated the variance reduction (VR) between the observed and synthetic seismograms, which is written as

$$VR = \left[1 - \frac{\sum_{k=1}^{N} \int \left(u_k^{\mathrm{obs}}(t) - u_k^{\mathrm{syn}}(t)\right)^2 dt}{\sum_{k=1}^{N} \int \left(u_k^{\mathrm{obs}}(t)\right)^2 dt}\right] \times 100\%, \tag{2}$$

where $u_k^{\mathrm{obs}}(t)$ and $u_k^{\mathrm{syn}}(t)$ are the observed and synthetic seismograms, respectively, and N is the number of the used stations.

We discarded possibly occurring cycle-skipping solutions when the difference in arrival times between t he observed and synthetic seismograms was larger than 0.35 s. The arrival times of the observed seismograms were estimated following Langet et al. (2014) as noted above. As already mentioned, those for the synthetic seismograms were measured when these absolute amplitudes first obtained 5% of a maximum absolute amplitude. Then, we determined the best CMT solution with the highest VR ($\mathrm{VR_{best}}$) from the remaining CMT solutions, which were obtained without cycle-skipping.

Finally, for the obtained CMT solutions, we estimated the uncertainties of the moment tensor solutions using a

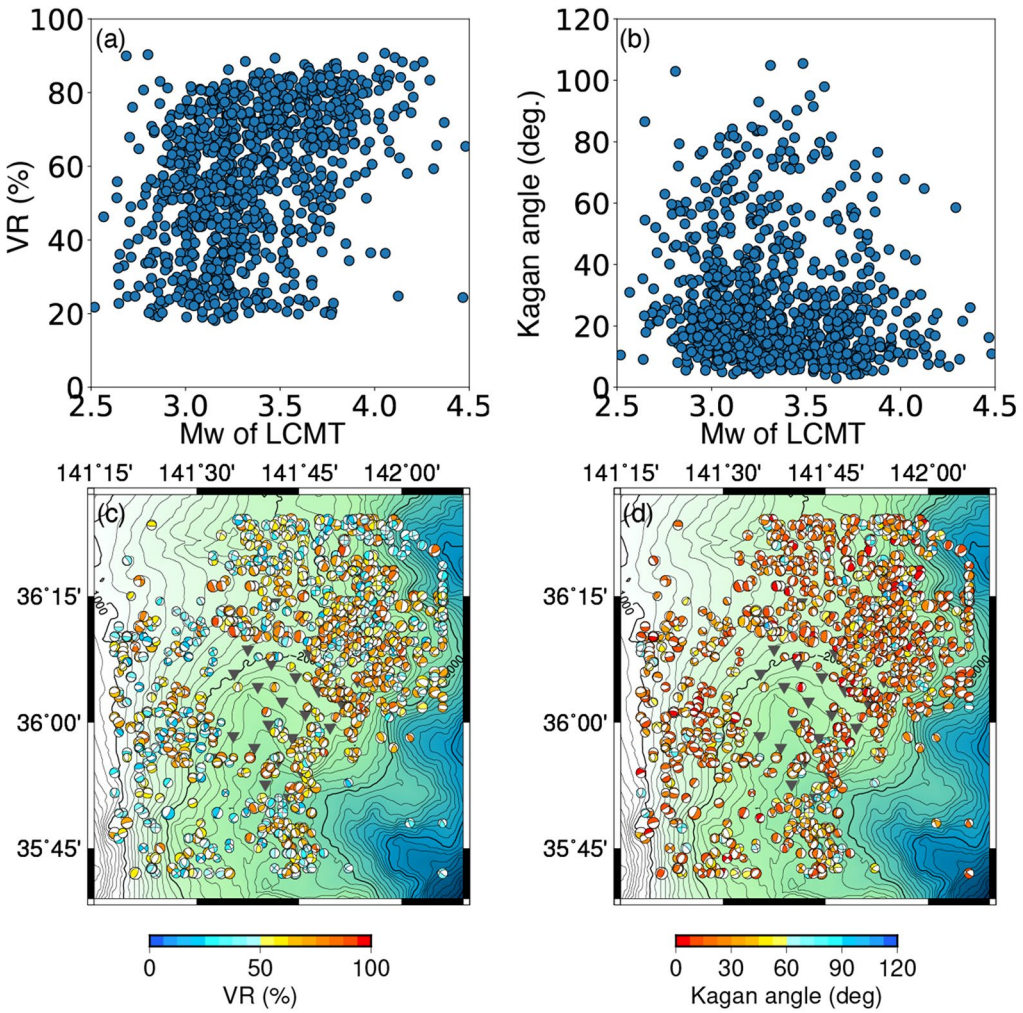

Fig. 2 **a** Moment magnitudes of the obtained CMT solutions against the VRs, and (**b**) the 68% confidence interval of Kagan angle by bootstrap results. **c** Spatial distribution of the VRs and **d** of the 68% confidence interval of Kagan angle

bootstrap method (e.g., Efron 1992; Zhan et al. 2012). We randomly selected stations that were used in CMT inversions, which allowed for overlapping and made 10000 sets of bootstrap samples. We performed the CMT inversion for each bootstrap samples, with a hypocenter fixed at the best CMT solution. We estimated the 68% confidence interval of the Kagan angle (Kagan 2007) from the distribution of these CMT solutions.

Results and discussion

We discarded CMT solutions whose VR_{best} was less than 40% (Fig. 2a, c) and whose 68% confidence interval of the Kagan angle by bootstrap results was larger than 30° (Fig. 2b, d). We obtained 536 CMT solutions for $2.5 \leq M_w \leq 4.5$ earthquakes. In addition, 87 of our CMT solutions achieved VR_{best} larger than 80%, although we did not use any station corrections, such as shifting the time windows or changing the amplitude factors. We obtained relatively small values of VR_{best} for earthquakes with smaller ($M_w \leq 3.5$) moment magnitudes because of the lower signal-to-noise ratio, even when the centroids were close to the OBS array. Successive occurrences of aftershocks within very short intervals following the 2011 Tohoku-oki earthquake could also cause noise in our single-event CMT inversion. The 68% confidence interval of the Kagan angle did not depend on the moment magnitude but on the spatial location. This Kagan angle tends to be large for earthquakes that occurred far from the OBS array because of the insufficient azimuthal coverage of the OBS stations.

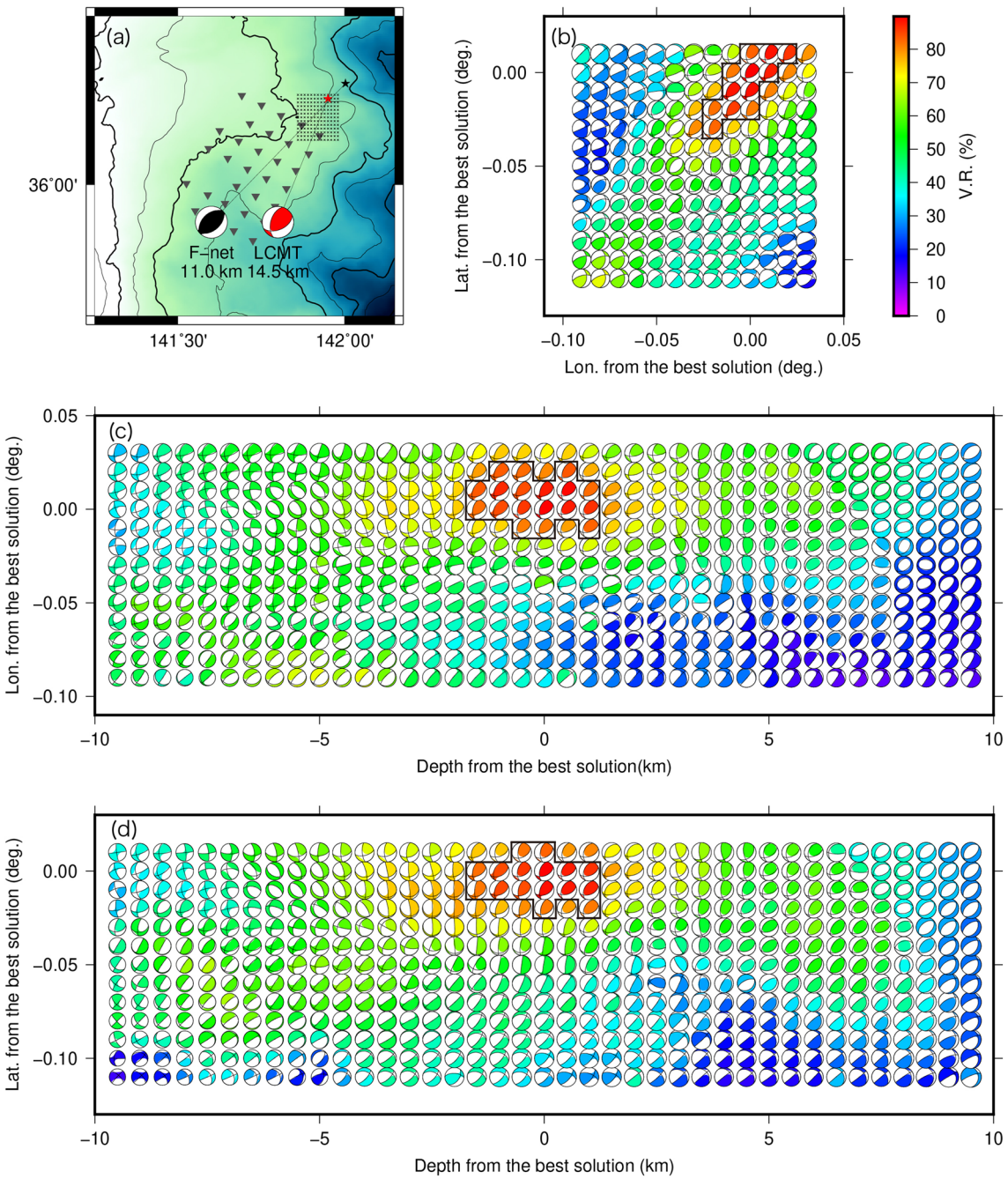

Fig. 3 Result of the CMT inversions for the earthquake (M_W4.0) that occurred at 9:06, March 16, 2011 (JST). **a** Centroid location of the earthquake and the OBS array. The red star shows the horizontal location of the best centroid with 14.5 km depth. The red focal mechanism shows the moment tensor of the best CMT solution. The black star indicates the horizontal location of the F-net MT solution with 11.0 km depth. The black focal mechanism shows the moment tensor of the F-net MT solution. The grey triangles show the stations of the OBS array. **b** Horizontal resolution of the CMT solution. The color of the focal mechanisms shows the VR. The region surrounded by the black line shows VR more than 90% from our best. **c** Depth resolution with longitudinal direction, and (**d**) with latitudinal direction

We significantly increased the spatial resolution using high-frequency data. Figure 3 shows an example of the inversion results for an earthquake that occurred on 9:06, March 16, 2011 (JST). Our solution was consistent with the F-net MT solution. The spatial distribution of VRs shows that the centroid was well-constrained,

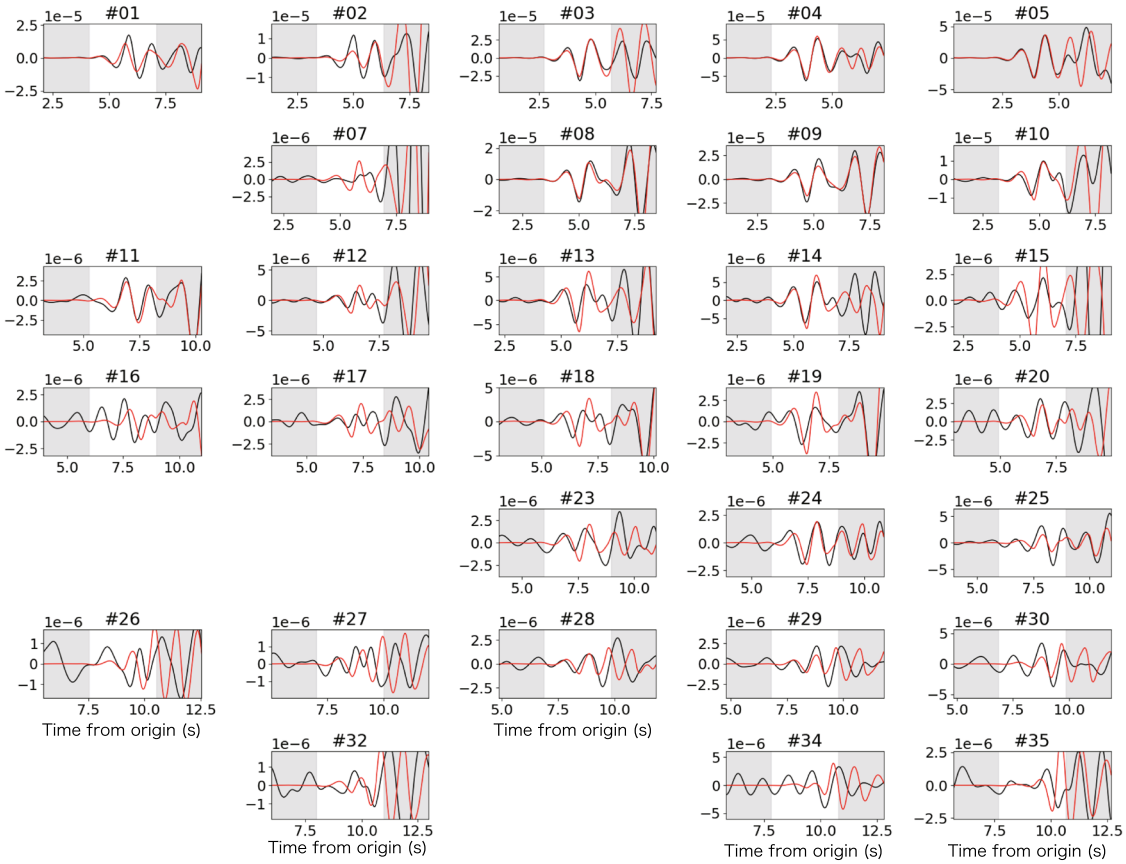

Fig. 4 Comparison of observed and synthetic seismograms for the earthquake ($M_W = 4.0$) that occurred at 9:06, March 16, 2011 (JST). The black and red lines show observed and synthetic seismograms, respectively. The station numbers are shown in Fig. 1b. The white-colored area shows the used time windows. Note that we did not use station #05, because the raw seismogram before applying the bandpass filter was saturated in 5 s from the beginning of the time window

with ~ 1 km for VRs exceeding 90% of VR_{best} (e.g., Kubota et al. 2017). In low-frequency CMT analyses using a 3-D seismic velocity model (e.g., Figs. 3 and 4 in Takemura et al. 2020), higher VRs appeared within depth ranges larger than 10 km. The depths with higher VRs from our CMT method were also constrained for earthquakes of other focal mechanisms (Additional file 1: Figs. S3–6).

The synthetic seismograms of our best CMT solution well-reproduced the observed seismograms (Fig. 4), not only for the P-wave in our 3-s CMT time windows but also for subsequent waves. For this earthquake, we did not use station #05 because of the saturation immediately after the time window, as noted in Sect. 3, but the direct P-wave observed in station #05 was reproduced by our CMT solution. Since Eq. (2), which minimize the VR overall, was used, some stations have the small VRs for each station (Additional file 1: Fig. S7). Such stations have a small amplitude and, therefore, a small contribution in Eq. (2).

We also calculated the VRs with various dip, strike, and rake angles to examine the estimation errors of the focal mechanisms (e.g., Takemura et al. 2020). Synthetic seismograms were calculated assuming double-couple sources and fixing centroids and seismic moments. Figure 5 illustrates the experiment. Although there is a trade-off between the rake and strike angles for this thrust earthquake, the dip angle was constrained. Higher VRs for dip angle in dip-rake and dip-strike planes ranged from 8° to 24°, where the VRs were larger than 90% of the maximum. The optimal dip angle is 16 °. For other types of mechanisms, similar characteristics of VR distributions were obtained (Additional file 1: Figs. S8–9).

The spatial distributions of the obtained CMT solutions are illustrated in Fig. 6. In the northeastern region, most of our CMT solutions of the earthquakes had thrust mechanisms (Figs. 6a–c, group A). Their mechanisms (dip and strike angles) and depths were consistent with the plate interface of the JIVSM, which

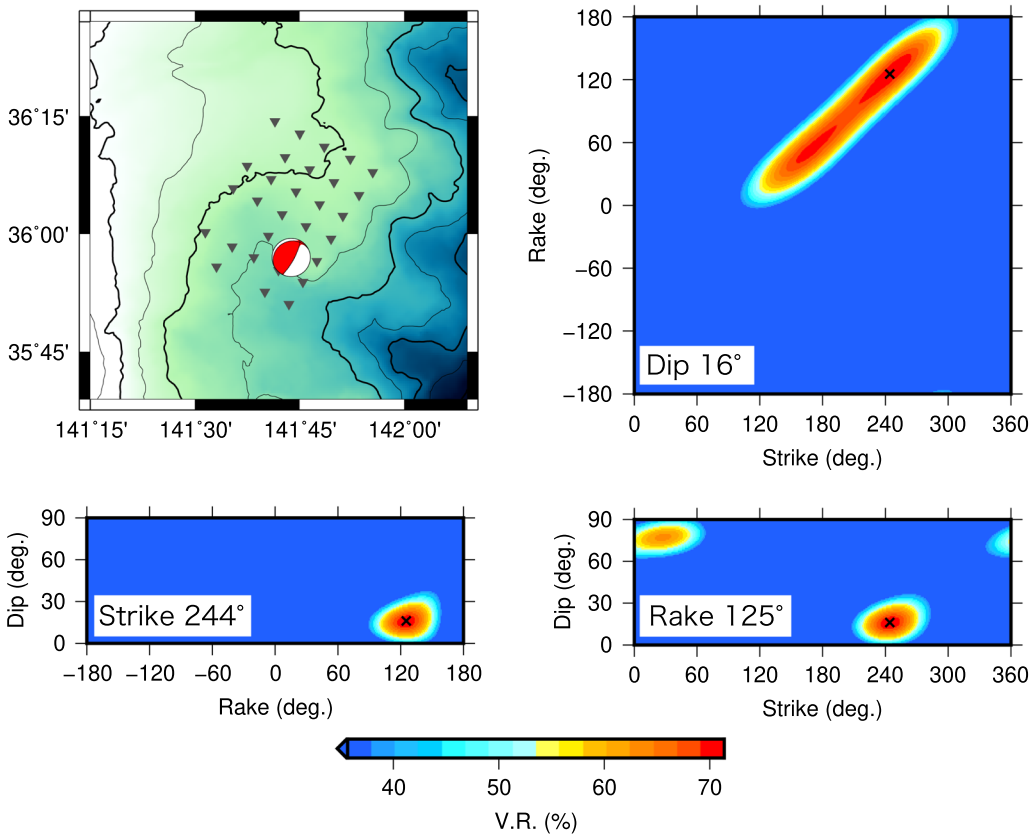

Fig. 5 Distribution of the VRs for the earthquake ($M_w = 3.8$) that occurred at 14:36, March 12, 2011 (JST), shown in the left top panel. Synthetic seismograms were calculated assuming double-couple sources, and fixing centroids and seismic moments. The strike, dip, and rake for the cross sections are the thrust fault of the obtained CMT solution

suggests that these earthquakes can be considered as interplate earthquakes. We found several shallow (10–15 km) earthquakes of normal-fault mechanisms at approximately 141.8°E and 36.1°N (Fig. 6a, c, group B). These normal-fault earthquakes are located shallower than thrust earthquakes. Although F-net MT solutions did not have sufficient depth resolution to distinguish between groups A and B, our high resolution centroid revealed the evident separation between the source regions of these normal-fault (group B) and interplate earthquakes (group A). In the other region, fewer earthquakes of thrust mechanisms occurred at the plate interface. Instead, in the northern region, our CMT solutions had strike-slip mechanisms at 25–35 km depths (Fig. 6a, b, group C), which are deeper than the plate interface. In the southwestern region, the earthquakes were characterized by normal-fault mechanisms within a depth range of 25–35 km (Fig. 6a, d, group D), which are also deeper than the plate interface. The earthquakes in the southernmost region are characterized by various types of mechanisms (Fig. 6a, e, group E). The group-E earthquakes are widely distributed in the vertical direction, in contrast to most group-A earthquakes, which are considered as the interplate earthquakes.

Comparison with previous focal-mechanism catalogs

We obtained 536 CMT solutions from $2.5 \leq M_w \leq 4.5$ earthquakes, whereas 209 F-net MT solutions were available in our analyzed period. The small number of F-net MT solutions is because F-net routine system based on the analysis of low-frequency (≤ 0.05 Hz) surface waves could not include $M_w \leq 3.5$ earthquakes. In our CMT inversion, using high-frequency data enabled us to obtain CMT solutions for smaller earthquakes.

For the 54 earthquakes with larger moment magnitudes, the CMT solutions were obtained in both the F-net MT analysis and this study. Although the spatial resolutions of F-net MT solutions are not high owing to the use of low-frequency waves, their focal mechanisms are expected to be less sensitive to the heterogeneous structure. To examine the stability of our CMT solutions, we calculated the Kagan angle between the F-net MT and the corresponding CMT solutions. We

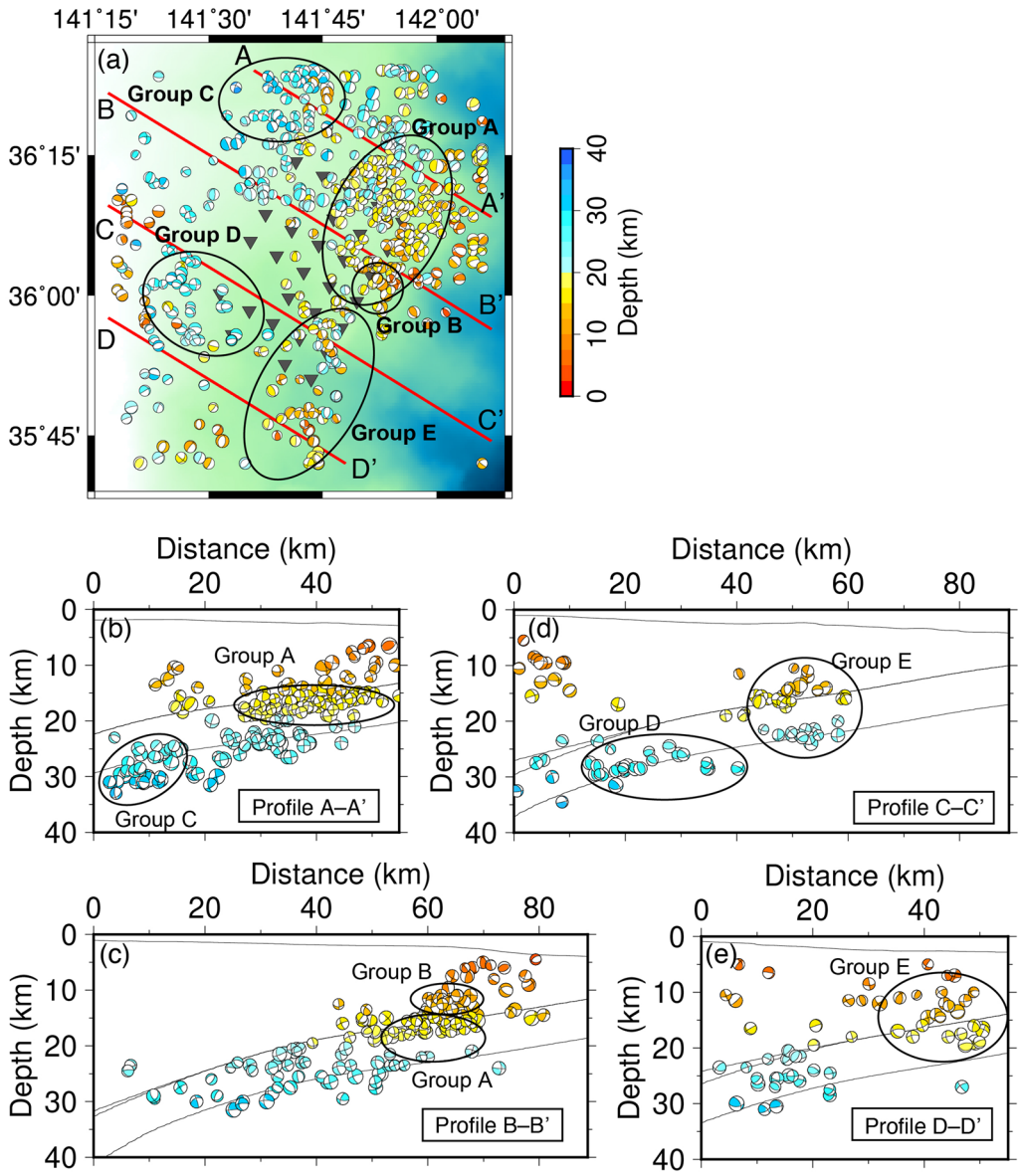

Fig. 6 **a** Spatial distribution of the obtained CMT solutions. The color of the focal mechanisms shows their depth. **b**–**e** Cross sections with the profiles of A–A', B–B', C–C', and D–D', respectively. The thin lines show the bathymetry, the upper surface and oceanic Moho of the Pacific Plate, and the upper surface of the Philippine Sea Plate (Koketsu et al. 2012)

also compared our CMT solutions with AQUA CMT and Asano et al. (2011). Because the numbers of AQUA and Asano's solutions within our target period are only 5 and 11, respectively, we only focused on comparisons between our CMT and F-net MT solutions. Since F-net routine MT analysis provides lower depth resolution and is conducted on the fixed epicenter determined by JMA, we focused only on the differences in the focal mechanisms between F-net MT and our CMT solutions. The obtained Kagan angles were smaller than 30° for most earthquakes, which suggests that our CMT solutions are consistent with F-net MT solutions (Fig. 7). However, large Kagan angles were obtained at approximately 142.1°E and 36.1°N. In addition to the insufficient azimuthal coverage, the focal depths of these earthquakes were presumably shallow, considering the subduction geometry. Thus, focal sphere coverage may be insufficient for accurate CMT

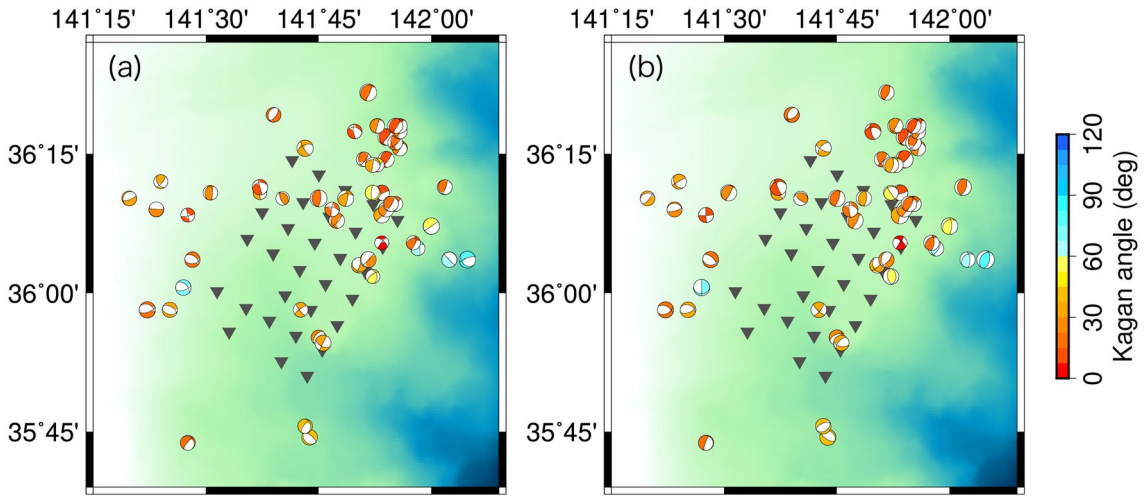

Fig. 7 Spatial distribution of Kagan angles. The colors of the moment tensors suggest the difference in Kagan angles between F-net MT and obtained CMT solutions. **a** Kagan angles with obtained and **b** with F-net MT solutions

estimation. In the following discussion, we discarded the CMT solutions obtained in this region.

Our centroid distribution mostly agrees with the hypocenters of Shinohara et al. (2011, 2012) as shown in Additional file 1: Fig. S10a, c. The hypocenters were determined using the P- and S-wave arrival times. It is known that the only use of the P-wave arrival times yields a lower depth resolution. However, our depths were consistent, although we did not include S-waves. This might be the result of including information on the amplitudes and a well-constrained 3-D structure model (Yamaya et al. 2021). The number of CMT solutions is larger than that of first-motion focal mechanisms by Shinohara et al. (2012), who used more OBS stations. Our CMT solutions were more consistent with the subducting Pacific Plate than their first-motion solutions. Directly following the 2011 Tohoku-oki earthquake, it was more difficult to read the first-motion polarities because of the coda waves from successive aftershocks. The intense aftershock activity caused a low signal-to-noise ratio, which obstructed manual phase identification for reading the first-motion polarities. Misreading of the first-motion polarities cause large uncertainty in the focal mechanisms, especially for the strike-dip mechanisms (Hardebeck and Shearer 2002). Our CMT inversion that includes the amplitude information in addition to the first-motion polarities might provide better constraints to the focal mechanisms without reading the first-arrival polarities. Correlations or other parameters in various catalogs are shown in Additional file 1: Figure S10.

Tectonic interpretations

Owing to the high-frequency analysis and the dense OBS array, we increased the number of CMT solutions for the aftershocks in the off Ibaraki region. Their spatial resolutions were also improved compared with conventional low-frequency CMT analysis. Consequently, the densities and accuracies of the focal mechanisms increased in both space and time. In this section, we discuss the tectonic interpretations of the aftershocks following the 2011 Tohoku-oki earthquake.

Most of the aftershocks occurring in the northern region of the OBS array are characterized by thrust mechanisms (group A in Fig. 6). To discuss the lateral distribution of the interplate earthquakes, we selected earthquakes with the thrust mechanisms whose Kagan angles with a typical interplate earthquake (strike = 195°, dip = 13°, rake = 90°) are less than 30 °. The selected earthquakes can be interpreted as interplate earthquakes (Fig. 8a). Their distributions were consistent with the region, where the active seismicity at the plate interface was obtained (Nakatani et al. 2015). These thrust earthquakes occurred in locations separated from the large slip area of the 2011 Ibaraki-oki earthquake (e.g., Kubo et al. 2013). The low seismicity of the thrust earthquakes at the large slip area of the 2011 Ibaraki-oki earthquake suggests that this earthquake released sufficient accumulated strain at the plate interface and consequently prohibited thrust earthquakes within the large slip area. These thrust earthquakes were also observed in locations separated from the tectonic tremors, which were estimated to occur at the up-dip side of the subducting seamount (e.g., Nishikawa et al. 2019; Kubo and Nishikawa

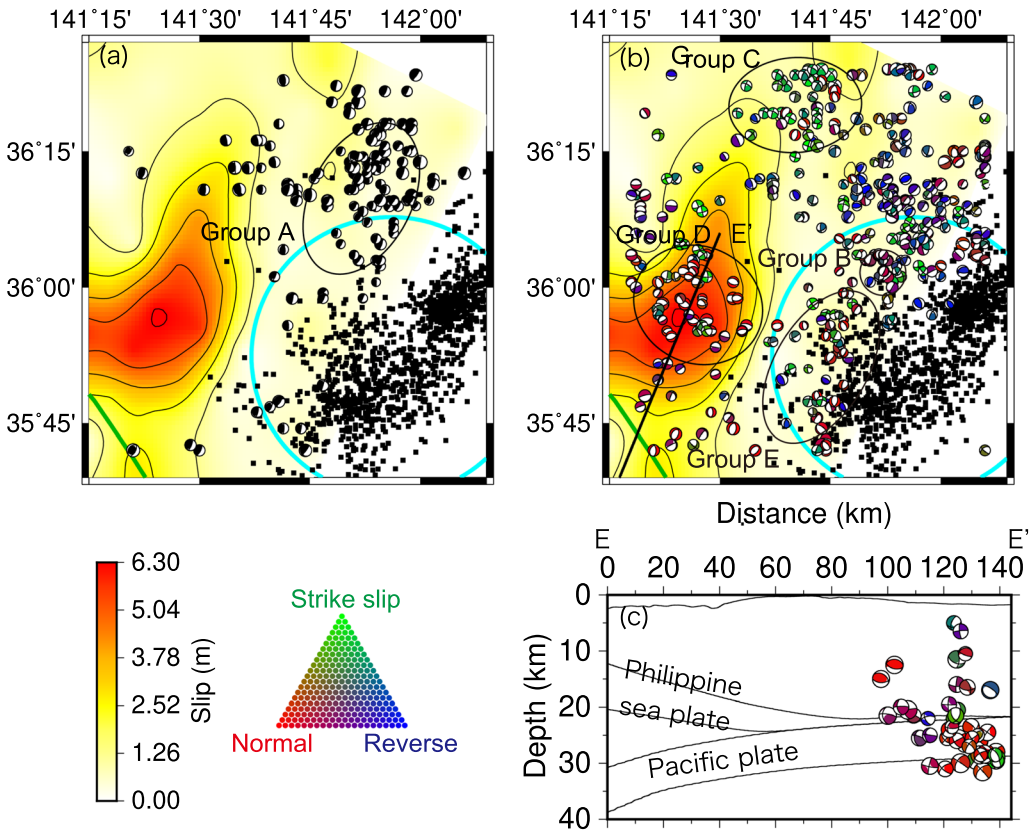

Fig. 8 **a** Spatial distribution of the thrust mechanisms. The black squares show the tectonic tremors detected by Nishikawa et al. (2019). The slip area of the 2011 Ibaraki-oki earthquake (Kubo et al. 2013) is also shown. The cyan circle shows the subducting seamount (Mochizuki et al. 2008). The green line shows the northeastern limit of the Philippine Sea Plate (Uchida et al. 2010). **b** Spatial distribution of the non-thrust mechanisms. The color of the focal mechanisms shows their type: red mechanisms are normal faults, blue mechanisms are reverse faults, and green mechanisms are strike-slip faults. **c** Cross section of the E–E' line, in which the point E is at 140.9° E and 34.9° N

2020). Tectonic tremors are slow earthquakes that are observed in the high-frequency (2–8 Hz) range (summarized in Obara & Kato 2016). These separations of interplate regular and slow earthquakes have also been reported in various subduction zones (e.g., Dixon et al. 2014; Takemura et al. 2020; Plata-Martínez et al. 2021). Slow earthquakes tend to be concentrated in the regions with weak locking strengths (e.g., Takemura et al. 2019). Our results agree that the tremor region can be considered as a weak locked zone, and consequently, accumulated stress may be insufficient to activate thrust-type regular earthquakes.

We colored the mechanism types not classified as the interplate earthquakes according to Frohlich (1992), as shown in Fig. 8b. The strike-slip mechanisms (group C) were obtained in the northern region, which is the northern part of the fault area of the 2011 Ibaraki-oki earthquake (M_W 6.8). From the east to the west region of this group, the northwest–southeast orientation of the maximum compressional axes rotates to the northeast–southwest. The systematically rotated principal axes seem to reflect the static stress change caused by the 2011 Ibaraki-oki earthquake. Previous studies have suggested that large earthquakes can rotate the orientation of the principal stress axes around their fault areas (e.g., Asano et al. 2011; Hasegawa et al. 2011; 2012; Yoshida et al. 2014). Recently, the spatio-temporal changes in the principal stress axes of focal mechanisms have revealed the initial differential stresses, which inform the fault strengths or the coupling strength at plate boundaries (e.g., Hardebeck and Okada 2018). Further investigation may provide us with insights into the original stress state before the 2011 Ibaraki-oki earthquake.

We obtained normal-fault earthquakes at depths greater than 20 km in the western region (group D in Fig. 8b, c). These centroid depths are deeper than the plate interface. We note that the F-net MT solutions also listed such normal-fault earthquakes with $M_w \geq 3.5$ following the 2011 Tohoku-oki earthquake. We propose a

possible effect of subduction of the Philippine Sea Plate on these normal-fault earthquakes. In this region, the northeastern edge of the Philippine Sea Plate has been estimated (e.g., Uchida et al. 2010; Nakahigashi et al. 2012). For other subduction zones, normal-fault earthquakes have been reported in the incoming oceanic plate prior to subduction. This is possibly due to the tensional stress field caused by plate bending of the subducting plate (e.g., Ranero et al. 2005). Especially in the Tohoku region, studies revealed that the overriding North American Plate might cause plate bending of the Pacific Plate beneath (e.g., Gamage et al. 2009; Obana et al. 2012, 2021). Similarly, the overriding Philippine Sea Plate might also cause plate bending of the Pacific Plate beneath, and consequently normal-fault earthquakes occur within the subducting Pacific Plate.

The most southern region, where the subducting seamount is imaged (e.g., Mochizuki et al. 2008), has various focal mechanisms (group E in Fig. 8b). Bootstrap analysis supported that the stable estimation of various focal mechanisms (Fig. 2d). Previous studies have also determined various types of focal mechanisms in the regions surrounding the subducting seamount (e.g., Bilek and Engdahl 2007). These observations suggest that a subducting seamount generates 3-D complex fractures in the overriding and subducting plates (e.g., Wang and Bilek 2011, 2014; Contreras-Reyes et al. 2015; Chesley et al. 2021). The existence of complex fractures is consistent with the complex topography of the upper crust of the overriding plate (Yamaya et al. 2021).

Our study found shallow (10–15 km) earthquakes of normal-fault mechanisms, which may also highlight the effect of the subducting seamount (group B in Fig. 8b). These earthquakes are tightly clustered, and the thrust fault earthquakes (group A) occurred at several kilometers below this cluster (Fig. 6c). The fault mechanisms of groups A and B were mostly reversed. It is known that such reversal fault slips (thrust and normal-fault earthquakes) with short separation distances rarely occur, but the first-arrival polarities also support this occurrence (Fig. 9).

We propose the effect of the subducting seamount on the generation of these normal-fault earthquakes. Recent numerical studies simulating mechanical coupling and hydrological processes have suggested that a simple shape of a subducting seamount can create a tensional stress field in the overriding plate (e.g., Sun et al. 2020). The compression of the overriding plate by a subducting seamount can increase the normal stress. In more detail, the observed normal-fault earthquakes are localized compared to the lateral size of the subducting seamount. A chain of seamounts existing on the incoming Pacific Plate seaward of the trench have a more complex shape than that assumed in the simulation by Sun et al. (2020). A more detailed shape of the seamounts may need to be considered to explain the localized normal-fault earthquakes.

Influence of array configuration on CMT inversion

In this study, we used a dense OBS array with a station interval of approximately 6 km. This station interval is smaller than that of a typical OBS array of 10–20 km. To examine the effect of array density, we conducted CMT inversion by changing the array density. The obtained CMT solution from the sparse array (12 km interval) agrees with that obtained using the dense OBS array (Fig. 10a). However, the CMT results exhibited high VRs over wider areas compared to those of the original dense array (Figs. 10b–d). This wider spatial distribution of the high VRs suggests that the CMT solutions determined by the sparser array reduce the spatial resolution to 5 km, which is five times longer than that of the original dense array. In this resolution, we could not discuss the depth distribution between the earthquakes of groups A and B.

Despite the low spatial resolution, the CMT analysis with the sparser array can provide accurate focal mechanisms, using P-wave arrival times to reject the cycle-skipping solutions. This examination suggests that CMT solutions can be obtained with short-period OBS arrays with typical station intervals. The analysis of OBS data to obtain focal mechanisms has conventionally been only using the first-arrival polarities, but CMT inversion can take the place of the first-arrival analysis. Recent developments in detailed seismic velocity structure models, numerical simulation codes of seismic wave propagation, and computational resources have enabled us to conduct CMT inversions without reading first-arrival polarities. Our CMT inversion can be conducted without precise first-arrival pickings. Using our CMT inversion, the systematic monitoring of offshore small-to-moderate earthquakes can be accomplished.

As OBS networks of both temporary and permanent placement have been developed along subduction zones (e.g., Cascadia Initiative: Toomey et al. 2014; DONET, S-net: Aoi et al. 2020), CMT analysis of the OBS networks will reveal more detailed stress fields beneath the ocean in the future. In this study, we only used P-waves, because S-waves are mostly saturated owing to the insufficient dynamic range of the OBSs. These saturated data compelled us to exclude S-waves from the analysis, but in general, incorporating S-waves will allow us to better constrain CMT solutions. Improving wider dynamic ranges of the OBSs or including other types of the seismometers, such as seismic accelerometers,

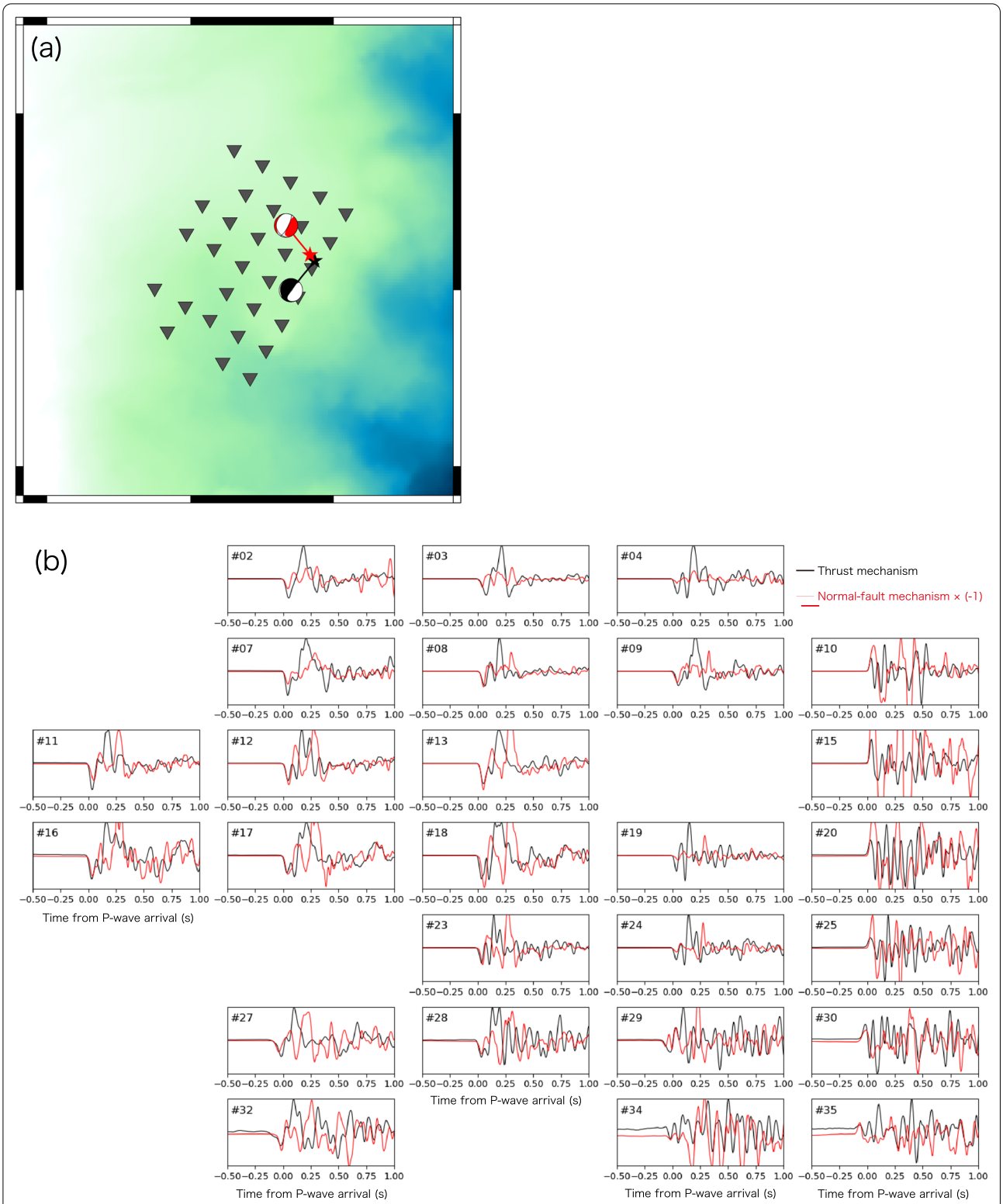

Fig. 9 Reversal fault pairs. **a** Black and red stars show locations of the thrust and normal-fault mechanisms for the earthquakes that occurred on April 12 and 30, 2011 (JST), respectively. The depths were 15 km and 12 km, respectively. **b** Raw seismogram comparison between the earthquakes. Black lines show the raw seismograms for the thrust mechanism, and red lines show the reversal amplitudes of those for the normal-fault mechanism

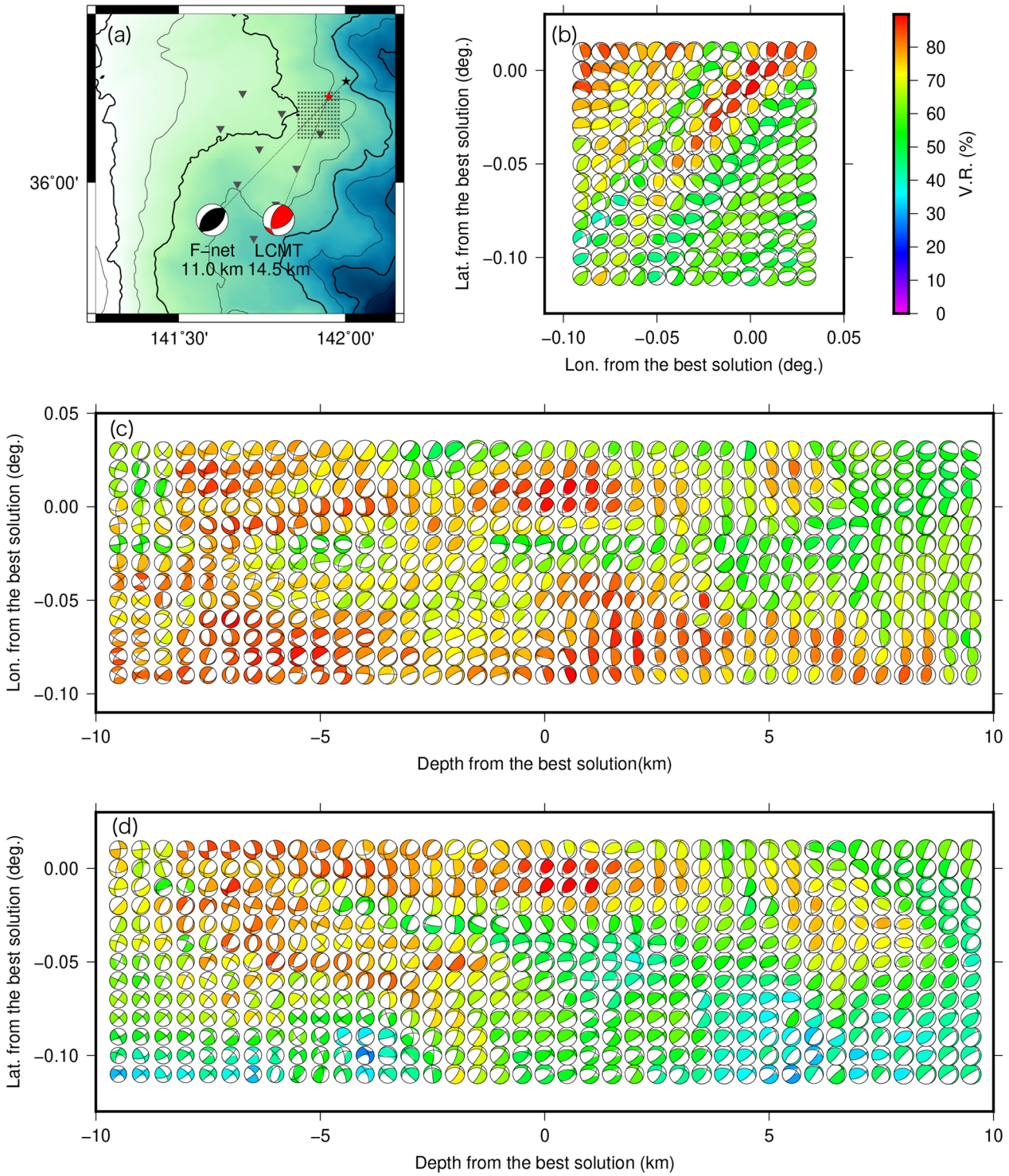

Fig. 10 Result of the CMT inversions for the earthquake that occurred at 9:06, March 16, 2011 (JST), using sparse OBS stations. Notations are the same as Fig. 3

will provide us to use both P- and S-waves in waveform analysis.

Conclusions

We determined CMT solutions of the aftershocks of the 2011 Tohoku-oki earthquake using the dense array of short-period OBSs in the off Ibaraki region. Our method based on Green's functions in the 3-D seismic velocity structure model can obtain CMT solutions for offshore earthquakes with M_w of 2.5–4.5. Our CMT solutions included smaller magnitude earthquakes than those obtained by the conventional low-frequency CMT method. Consequently, we obtained 536 CMT solutions, which were larger than those in the catalogs of previous publications. Our CMT solutions reflect the complex stress field in the off Ibaraki region.

The obtained CMT solutions are as follows: (1) thrust-type interplate earthquakes in locations separated with the fault area of the 2011 Ibaraki-oki earthquake and the tectonic tremors; (2) intraslab strike-slip earthquakes located north of the fault area of the 2011 Ibaraki-oki earthquake; (3) intraslab normal-fault earthquakes, which suggest a tensional stress field at the subducting Pacific Plate due to the plate bending by the overriding Philippine Sea Plate; (4) earthquakes with various focal mechanisms above the subducting seamount, which suggest 3-D complex fractures caused by the subducting seamount; and (5) shallow normal-fault earthquakes possibly caused by the subducting seamount. Our CMT inversion using short-period OBSs can be applied to other offshore regions, which has sufficient potential to reveal the detailed stress fields in offshore regions.

Abbreviations

3-D: Three-dimensional; AQUA: Accurate and QUick Analysis system for source parameters; CMT: Centroid moment tensor; DONET: Dense Ocean floor Network system for Earthquake and Tsunamis; FDM: Finite-difference method; F-net: Full-range seismograph network; JIVSM: Japan Integrated Velocity Structure Model; JMA: Japan Meteorological Agency; OBS: Ocean bottom seismometer; M_{JMA}: JMA-scale magnitude; M_w: Moment magnitude; MT: Moment tensor; OpenSWPC: Open-source seismic wave propagation code; S-net: Seafloor observation Network for Earthquake and Tsunamis along the Japan Trench; The 2011 Tohoku-oki earthquake: The 2011 off the Pacific coast of Tohoku earthquake; VR: Variance Reduction.

Supplementary Information

The online version contains supplementary material available at https://doi.org/10.1186/s40623-022-01721-3.

Additional file1: Fig. S1. Effect of the source time function. (a) Seismograms filtered with 0.4–1.0 Hz. Black lines show the synthetic seismograms using delta-function-type source time function. Red lines show those using the finite-duration source time function, which is evaluated using the empirical scaling low against moment magnitudes (Ekstrom et al., 2012). (b) Assumed duration through moment magnitudes. **Fig. S2.** (a) Observed seismograms filtered with 4.0–10.0 Hz and obtained its kurtosis gradient at station #07 for the earthquake that occurred at 17:27, October 25, 2010 (JST). (b) Zoomed-in view of the same waveforms around the selected arrival time. **Fig. S3.** Result of the CMT inversions for the earthquake that occurred at 11:01, March 16, 2011 (JST). Notations are the same as Figure 3. **Fig. S4.** Result of the CMT inversions for the earthquake that occurred at 21:51, March 30, 2011 (JST). Notations are the same as Figure 3. **Fig. S5.** Result of the CMT inversions for the earthquake that occurred at 19:57, April 8, 2011 (JST). Notations are the same as Figure 3. **Fig. S6.** Result of the CMT inversions for the earthquake that occurred at 11:53, April 13, 2011 (JST). Notations are the same as Figure 3. **Fig. S7.** Same as Figure 4 but with VR for each station. **Fig. S8.** Distribution of VRs for the earthquake M_W=3.7 that occurred at 21:51, March 20, 2011 (JST). The strike, dip, and rake for the cross sections are the high dip-angle fault of the obtained CMT solution. Notations are the same as figure 5. **Fig. S9.** Distribution of VRs for earthquake (M_W=4.2) that occurred at 11:29, April 15, 2011 (JST). Notations are the same as figure 5. **Fig. S10.** Comparisons of our centroids with (a) Shinohara et al. (2011, 2012) and (b) JMA. Comparison of our depths with (c) Shinohara et al. (2011, 2012), (d) F-net MT and (e) JMA. Comparison of our M_W with (f) M_W of F-net MT and (g) M_{JMA} by JMA.

Acknowledgements

We thank NIED and JMA for providing the earthquake catalog. We thank Youichi Asano and Katsuhiko Shiomi for providing the CMT catalogs. We thank Hisahiko Kubo for providing the fault slip model and fruitful discussing. Numerical simulations of seismic wave propagation were conducted using the Oakforest-PACS system at the Information Technology Center, The University of Tokyo. We also acknowledge Babak Hejrani, an anonymous reviewer, editor Naoki Uchida, and editor-in-chief Takeshi Sagiya, for careful reviewing and constructive comments, which helped to improve the manuscript. This research is a part of the PhD thesis of Lina Yamaya (Yamaya 2022).

Author contributions

LY conducted data processing and CMT solutions with assistance from KM, TA and ST. KM, MS and TY arranged the OBS observation. LY, KM and TA contribute to the tectonic interpretation. ST supported the numerical simulation of the seismic wave propagation. LY drafted the first version of the manuscript. All authors read and approved the final manuscript.

Funding

This study is supported by JSPS KAKENHI Grant Number 19J20692, 22K20388, and JP21H05205 in Grant-in-Aid for Transformative Research Areas (A) "Science of Slow-to-Fast Earthquakes". This study is also supported by MEXT Project for Seismology toward Research Innovation with Data of Earthquake (STAR-E) Grant Number JPJ010217. This work used computational resources of Oakforest-PACS provided by The University of Tokyo through the HPCI System Research Project (Project ID: hp120308) and ERI JURP 2021-S-B102.

Availability of data and materials

Our CMT solutions and the 3-D seismic velocity structure model are available at https://doi.org/10.5281/zenodo.6999136. The seismograms used in this manuscript are available from KM on request.

Declarations

Ethics approval and consent to participate

Not applicable.

Consent for publication

Not applicable.

Competing interests

The authors declare that they have no competing interests.

Author details

[1]Earthquake Research Institute, The University of Tokyo, 1-1-1, Yayoi, Tokyo, Bunkyo-Ku, Japan. [2]National Research Institute for Earth Science and Disaster Resilience, 3-1, Tennodai, Tsukuba, Ibaraki 305-0006, Japan.

Received: 9 March 2022 Accepted: 16 October 2022
Published: 8 November 2022

References

Aoi S, Asano Y, Kunugi T, Kimura T, Uehira K, Takahashi N, Ueda H, Shiomi K, Matsumoto T, Fujiwara H (2020) MOWLAS: NIED observation network for earthquake, tsunami and volcano. Earth Planet Space 72:1–31. https://doi.org/10.1186/s40623-020-01250-x

Asano Y, Saito T, Ito Y, Shiomi K, Hirose H, Matsumoto T, Aoi S, Hori S, Sekiguchi S (2011) Spatial distribution and focal mechanisms of aftershocks of the 2011 off the Pacific coast of Tohoku earthquake. Earth Planet Space 63:669–673. https://doi.org/10.5047/eps.2011.06.016

Bilek SL, Engdahl ER (2007) Rupture characterization and aftershock relocations for the 1994 and 2006 tsunami earthquakes in the Java subduction zone. Geophys Res Lett. https://doi.org/10.1029/2007GL031357

Brocher TM (2005) Empirical relations between elastic wavespeeds and density in the Earth's crust. B Seismol Soc Am 95:2081–2092

Brocher TM (2008) Key elements of regional seismic velocity models for long period ground motion simulations. J Seismol 12:217–221

Chesley C, Naif S, Key K, Bassett D (2021) Fluid-rich subducting topography generates anomalous forearc porosity. Nature 595:255–260

Contreras-Reyes E, Ruiz JA, Becerra J, Kopp H, Reichert C, Maksymowicz A, Arriagada C (2015) Structure and tectonics of the central Chilean margin (31°–33° S): Implications for subduction erosion and shallow crustal seismicity. Geophys J Int 203:776–791

Dixon TH, Jiang Y, Malservisi R, McCaffrey R, Voss N, Protti M, Gonzalez V (2014) Earthquake and tsunami forecasts: Relation of slow slip events to subsequent earthquake rupture. Proc Natl Acad Sci 111:17039–17044

Efron B (1992) Bootstrap methods: another look at the jackknife. In: Kotz S, Johnson NL (eds) Breakthroughs in statistics. Springer, New York, pp 569–593

Ekström G, Nettles M, Dziewoński AM (2012) The global CMT project 2004–2010: centroid-moment tensors for 13,017 earthquakes. Phys Earth Planet Inter 200:1–9

Frohlich C (1992) Triangle diagrams: ternary graphs to display similarity and diversity of earthquake focal mechanisms. Phys Earth Planet Inter 75:193–198

Fukuyama E, Ishida M, Drege DS, Kawai H (1998) Automated seismic moment tensor determination by using on-line broadband seismic waveforms. Zisin 51:149–156

Gamage SS, Umino N, Hasegawa A, Kirby SH (2009) Offshore double-planed shallow seismic zone in the NE Japan forearc region revealed by sP depth phases recorded by regional networks. Geophys J Int 178:195–214

Hardebeck JL, Okada T (2018) Temporal stress changes caused by earthquakes: a review. J Geophys Res 123:1350–1365

Hardebeck JL, Shearer PM (2002) A new method for determining first-motion focal mechanisms. B Seismol Soc Am 92:2264–2276

Hasegawa A, Yoshida K, Okada T (2011) Nearly complete stress drop in the 2011 M w 9.0 off the Pacific coast of Tohoku earthquake. Earth Planet Space 63:703–707. https://doi.org/10.5047/eps.2011.06.007

Hasegawa A, Yoshida K, Asano Y, Okada T, Iinuma T, Ito Y (2012) Change in stress field after the 2011 great Tohoku-Oki earthquake. Earth Planet Sci Lett 355:231–243

Hejrani B, Tkalčić H (2019) The 20 May 2016 Petermann Ranges earthquake: centroid location, magnitude and focal mechanism from full waveform modelling. Aust J Earth Sci 66:37–45

Hejrani B, Tkalčić H (2020) Resolvability of the centroid-moment-tensors for shallow seismic sources and improvements from modelling high-frequency waveforms. J Geophys Res 125:1–31

Hejrani B, Tkalčić H, Fichtner A (2017) Centroid moment tensor catalogue using a 3-D continental scale earth model: application to earthquakes in Papua New Guinea and the Solomon islands. J Geophys Res 122:5517–5543

Kagan YY (2007) Simplified algorithms for calculating double-couple rotation. Geophys J Int 171:411–418

Koketsu K, Miyake H, Suzuki H 2012 Japan Integrated Velocity Structure Model Version 1, Proc 15th World Conf Earthq Eng. p1–4

Kubo H, Nishikawa T (2020) Relationship of preseismic, coseismic, and postseismic fault ruptures of two large interplate aftershocks of the 2011 Tohoku earthquake with slow-earthquake activity. Sci Rep 10:1–10

Kubo A, Fukuyama E, Kawai H, Nonomura K (2002) NIED seismic moment tensor catalogue for regional earthquakes around Japan: quality test and application. Tectonophysics 356:23–48

Kubo H, Asano K, Iwata T (2013) Source-rupture process of the 2011 Ibaraki-oki, Japan, earthquake (Mw 79) estimated from the joint inversion of strong-motion and GPS data: relationship with seamount and Philippine sea plate. Geophys Res Lett 40:3003–3007

Kubota T, Saito T, Suzuki W, Hino R (2017) Estimation of seismic centroid moment tensor using ocean bottom pressure gauges as seismometers. Geophys Res Lett. https://doi.org/10.1002/2017GL075386

Langet N, Maggi A, Michelini A, Brenguier F (2014) Continuous kurtosis-based migration for seismic event detection and location, with application to Piton de la Fournaise Volcano, La Reunion. B Seismol Soc Am 104:229–246

Lay T, Ammon CJ, Kanamori H, Xue L, Kim MJ (2011) Possible large near-trench slip during the 2011 Mw 9.0 off the Pacific coast of Tohoku earthquake. Earth Planets Space 63:687–692. https://doi.org/10.5047/eps.2011.05.033

Lister G, Tkalčić H, Hejrani B, Koulali A, Rohling E, Forster M, McClusky S (2018) Lineaments and earthquake ruptures on the East Japan megathrust. Lithosphere 10:512–522

Maeda T, Takemura S, Furumura T (2017) OpenSWPC: an open-source integrated parallel simulation code for modeling seismic wave propagation in 3D heterogeneous viscoelastic media. Earth Planets Space 69:1–20. https://doi.org/10.1186/s40623-017-0687-2

Matsumura M, Ito Y, Kimura H, Obara K, Sekiguchi S, Hori S (2006) Development of accurate and quick analysis system for source parameters (AQUA). Zisin 59:167–184

Mochizuki K, Yamada T, Shinohara M, Yamanaka Y, Kanazawa T (2008) Weak interplate coupling by seamounts and repeating M~ 7 earthquakes. Science 321:1194–1197

Nakahigashi K, Shinohara M, Mochizuki K, Yamada T, Hino R, Sato T, Uehira K, Ito Y, Murai Y, Kanazawa T (2012) P-wave velocity structure in the southernmost source region of the 2011 Tohoku earthquakes, off the Boso Peninsula, deduced by an ocean bottom seismographic survey. Earth Planets Space 64:1149–1156. https://doi.org/10.5047/eps.2012.06.006

Nakamura T, Takenaka H, Okamoto T, Ohori M, Tsuboi S (2015) Long-period ocean-bottom motions in the source areas of large subduction earthquakes. Sci Rep 5:1–10

Nakatani Y, Mochizuki K, Shinohara M, Yamada T, Hino R, Ito Y, Murai Y, Sato T (2015) Changes in seismicity before and after the 2011 Tohoku earthquake around its southern limit revealed by dense ocean bottom seismic array data. Geophys Res Lett 42:1384–1389

Nishikawa T, Matsuzawa T, Ohta K, Uchida N, Nishimura T, Ide S (2019) The slow earthquake spectrum in the Japan Trench illuminated by the S-net seafloor observatories. Science 365:808–813

Noguchi S, Maeda T, Furumura T (2016) Ocean-influenced Rayleigh waves from outer-rise earthquakes and their effects on durations of long-period ground motion. Geophys J Int 205:1099–1107

Obana K, Fujie G, Takahashi T, Yamamoto Y, Nakamura Y, Kodaira S, Takahashi N, Kaneda Y, Shinohara M (2012) Normal- faulting earthquakes beneath the outer slope of the Japan Trench af- ter the 2011 Tohoku earthquake: Implications for the stress regime in the incoming Pacific plate. Geophys Res Lett. https://doi.org/10.1029/2012GL050399

Obana K, Fujie G, Yamamoto Y, Kaiho Y, Nakamura Y, Miura S, Kodaira S (2021) Seismicity around the trench axis and outer-rise region of the southern Japan Trench, south of the main rupture area of the 2011 Tohoku-oki earthquake. Geophys J Int 226:131–145

Obara K, Kato A (2016) Connecting slow earthquakes to huge earthquakes. Science 353:253–257

Okamoto T, Takenaka H, Nakamura T (2018) Evaluation of accuracy of synthetic waveforms for subduction-zone earthquakes by using a land–ocean unified 3D structure model. Earth Planets Space 70:1–10. https://doi.org/10.1186/s40623-018-0871-z

Plata-Martínez R, Ide S, Shinohara M, Garcia ES, Mizuno N, Dominguez LA, Taira T, Yamashita Y, Toh A, Yamada T, Real J, Husker A, Ito Y (2021) Shallow slow earthquakes to decipher future catastrophic earthquakes in the Guerrero seismic gap. Nature Com 12:1–8

Ranero CR, Villaseñor A, Phipps Morgan J, Weinrebe W (2005) Relationship between bend-faulting at trenches and intermediate-depth seismicity. Geochem Geophys Geosyst. https://doi.org/10.1029/2005GC000997
Sato H, Fehler M, Maeda T (2012) Seismic wave propagation and scattering in the heterogeneous earth structure, 2nd edn. Springer-Verlag, Berlin
Shapiro NM, Campillo M, Singh SK, Pacheco J (1998) Seismic channel waves in the accretionary prism of the Middle America Trench. Geophys Res Lett 25:101–104
Shinohara M, Yamada T, Nakahigashi K, Sakai S, Mochizuki K, Uehira K, Ito Y, Azuma R, Kaiho Y, No T, Shiobara H, Hino R, Murai Y, Yakiwara H, Sato T, Machida Y, Shinbo T, Isse T, Miya- Machi H, Obana K, Takahashi N, Kodaira S, Kaneda Y, Hirata K, Yoshikawa S, Obara K, Iwasaki T, Hirata N (2011) Aftershock observation of the 2011 off the Pacific coast of Tohoku earthquake by using ocean bottom seismometer network. Earth Planet Space 63:835–840. https://doi.org/10.5047/eps.2011.05.020
Shinohara M, Machida Y, Yamada T, Nakahigashi K, Shinbo T, Mochizuki K, Murai Y, Hino R, Ito Y, Sato T, Shiobara H, Uehira K, Yakiwara H, Obana K, Takahashi N, Kodaira S, Hirata K, Tsushima H, Iwasaki T (2012) Precise aftershock distribution of the 2011 off the Pacific coast of Tohoku Earthquake revealed by an ocean-bottom seismometer network. Earth Planets Space 64:1137–1148. https://doi.org/10.5047/eps.2012.09.003
Shipboard Scientific Party (2000) Leg 186 summary. Proc Ocean Drill Program Initial Rep 186:1–37
Sipkin SA (1982) Estimation of earthquake source parameters by the inversion of waveform data: synthetic waveforms. Phys Earth Planet Inter 30:242–259
Sun T, Saffer D, Ellis S (2020) Mechanical and hydrological effects of seamount subduction on megathrust stress and slip. Nat Geosci 13:249–255
Takemura S, Kobayashi M, Yoshimoto K (2016) Prediction of maximum P- and S-wave amplitude distribution incorporating frequency- and distance-dependent characteristics of the observed apparent radiation patterns. Earth Planet Space 68:166. https://doi.org/10.1186/s40623-016-0544-8
Takemura S, Noda A, Kubota T, Asano Y, Matsuzawa T, Shiomi K (2019) Migrations and clusters of shallow very low frequency earthquakes in the regions surrounding shear stress accumulation peaks along the Nankai Trough. Geophys Res Lett 46:11830–11840
Takemura S, Okuwaki R, Kubota T, Shiomi K, Kimura T, Noda A (2020) Centroid moment tensor inversions of offshore earthquakes using a three-dimensional velocity structure model: slip distributions on the plate boundary along the Nankai Trough. Geophys J Int 222:1109–1125
Takemura S, Yoshimoto K, Shiomi K (2021) Long-period ground motion simulation using centroid moment tensor inversion solutions based on the regional three-dimensional model in the Kanto region Japan. Earth Planet Space 73:1–18. https://doi.org/10.1186/s40623-020-01348-2
Toomey DR, Allen RM, Barclay AH, Bell SW, Bromirski PD, Carlson RL et al (2014) The Cascadia Initiative: a sea change in seismological studies of subduction zones. Oceanography 27:138–150
Tsuru T, Park JO, Miura S, Kodaira S, Kido Y, Hayashi T (2002) Along-arc structural variation of the plate boundary at the Japan trench margin: Implication of interplate coupling. J Geophys Res 107:2357. https://doi.org/10.1029/2001JB001664
Uchida N, Matsuzawa T, Nakajima J, Hasegawa A (2010) Subduction of a wedge-shaped Philippine sea plate beneath Kanto, central Japan, estimated from converted waves and small repeating earthquakes. J Geophys Res. https://doi.org/10.1029/2009JB006962
Volk O, Shani-Kadmiel S, Gvirtzman Z, Tsesarsky M (2017) 3D Effects of sedimentary wedges and subsurface canyons: Ground-motion amplification in the Israeli coastal plain. B Seismol Soc Am 107:1324–1335
Wang K, Bilek SL (2011) Do subducting seamounts generate or stop large earthquakes? Geology 39:819–822
Wang K, Bilek SL (2014) Invited review paper: fault creep caused by subduction of rough seafloor relief. Tectonophysics 610:1–24
Wang X, Zhan Z (2020) Moving from 1-D to 3-D velocity model: automated waveform-based earthquake moment tensor inversion in the Los Angeles region. Geophys J Int 220:218–234
White LT, Rawlinson N, Lister GS, Waldhauser F, Hejrani B, Thompson DA, Tanner D, Macpherson C, Tkalčić H, Morgan JP (2019) Earth's deepest earthquake swarms track fluid ascent beneath nascent arc volcanoes. Earth Planet Sci Lett 521:25–36
Yamaya L, Mochizuki K, Akuhara T, Nishida K (2021) Sedimentary Structure Derived From Multi-ModeAmbient Noise Tomography With Dense OBS Network at the Japan Trench. J Geophys Res, https://agupubs.onlinelibrary.wiley.com/doi/full/10.1029/2021JB021789 126, e2021JB021789
Yamaya L (2022) Complex stress state of the off Ibaraki region inferred from CMT analysis of dense OBS array data using 3-D velocity structure. PhD thesis of the University of Tokyo, Japan
Yoshida K, Hasegawa A, Okada T, Iinuma T (2014) Changes in the stress field after the 2008 M7. 2 Iwate-Miyagi Nairiku earthquake in northeastern Japan. J Geophys Res 119:9016–9030
Zhan Z, Helmberger D, Simons M, Kanamori H, Wu W, Cubas N, Duputel Z, Chu R, Tsai V, Avouac J, Hudnut KW, Ni S, Hetland E, Culaciati FHO (2012) Anomalously steep dips of earthquakes in the 2011 Tohoku-Oki source region and possible explanations. Earth Planet Sci Lett 353:121–133

Publisher's Note